Interplay of viscosity and wettability controls fluid displacement in porous media

Saideep Pavuluri,[1] Ran Holtzman [,2] Luqman Kazeem [,1] Malyah Mohammed,[1] Thomas Daniel Seers [,1] and Harris Sajjad Rabbani [1,*]

[1]*Department of Petroleum Engineering, Texas A&M University at Qatar,*
Education City, P.O. Box 23874, Doha, Qatar
[2]*Fluid and Complex Systems Research Centre, Coventry University, Coventry CV12NL, United Kingdom*

Direct numerical simulations are used to elucidate the interplay of wettability and fluid viscosities on immiscible fluid displacements in a heterogeneous porous medium. We classify the flow regimes using qualitative and quantitative analysis into viscous fingering (low M, M being the viscosity ratio—described as ratio of fluid viscosity of injected by defending phases), compact displacement (high M), and an intermediate transition regime ($M \approx 1$). We use stability analysis to obtain theoretical phase boundaries between these regimes, which agree well with our analyses. At the macroscopic (sample) scale, we find that wettability strongly controls the threshold M (at which the regimes change). At the pore scale, wettability alters the dominant pore-filling mechanism. At very small M (viscous fingering regime), smaller pore spaces are preferentially invaded during imbibition, with flow of films of invading fluid along the pore walls. In contrast, during drainage, bursts result in filling of pores irrespective of their size. As M increases, the effect of wettability decreases as cooperative filling becomes the dominant mechanism regardless of wettability. This suggest that for imbibition at a given contact angle, decreasing M is associated with change in effective wetting from neutral-wet (cooperative filling) to strong-wet (film flow).

I. INTRODUCTION

Fundamental understanding of immiscible fluid-fluid displacements in porous media is vital for the safe and efficient operation of a large number of engineering applications. Examples include sequestration of carbon dioxide [1,2], the fate of nonaqueous phase liquid contaminants (NAPLs) in groundwater [3,4] and their remediation [5], geothermal energy [6,7], and extraction of hydrocarbons [8,9]. The displacement patterns are controlled by the interplay of capillary, viscous, inertial and gravitational forces, which in turn are controlled by a wide range of parameters, including flow rates, fluid properties (viscosity, density, surface tension), wettability, and medium properties (pore sizes, shapes, and connectivity) [10].

The classical phase diagram of fluid displacement regimes predicts the transition between compact displacements, viscous fingering, and capillary fingering patterns considering the capillary number Ca (ratio of viscous to capillary forces) and viscosity ratio M [11,12]. These seminal works

---

*harris.rabbani@qatar.tamu.edu

did not consider however the effect of wettability—the affinity of one fluid relative to another to adhere to the solid surface, measured via the contact angle θ. References [11,12] considered only the extreme cases of drainage and imbibition, that is the displacement of a perfectly nonwetting and wetting fluid, respectively. Recent works however expose the crucial impact of wettability, showing it substantially affects the pore filling mechanisms and thus the displacement patterns [13–20]. Furthermore, Ref. [17] has shown that the displacement of immiscible fluids depend on the effective wettability rather than on the surface wettability. In addition to the microscopic description of the contact angle, the orientation of the pore spaces dictates the effective wettability of the system.

While the combined impact of Ca and θ on the fluid displacement patterns has been extensively researched, there exist limited studies that focused on the impact of M and θ on deciphering multiphase flows through porous media. Only recently, a few studies used numerical simulations to include the effect of wettability on displacement morphology. Primkulov *et al.* [21] used dynamic pore network modeling to decipher the interplay between wettability, viscosities, and flow rates, extending the classical phase diagram in Ref. [11]. The authors considered an idealized porous medium made of cylindrical pillars, for which analytical expressions providing the advancement of the meniscus via various filling mechanisms can be established [22]. Lattice Boltzmann (LB) simulations were used to study the impact of wettability and viscosity on the displacement efficiency for viscous fingering, on a similar idealized medium [23]. A more realistic 3D pore geometry, extracted from from micro-CT images of sandstone, was used in LB simulations to study how wettability and geometrical pore-scale heterogeneity affects the displacement, for two different viscosity ratios, favorable and unfavorable ($M \gg 1$ and $M \ll 1$, respectively) [24]. These works showed a transition from viscous fingering (VF) to compact displacement (CD) with increasing M.

Here, we extend the previous studies of Refs. [21,23,24] by systematically exploring the synergistic relationships between wettability and fluid viscosities in a geologically realistic medium under viscous-dominated flow. We use direct numerical simulations (DNS), which allow consideration of the physics (solving the fundamental flow equations) for the intricate pore geometry derived from a micro-CT image of a sand pack. The high spatial and temporal resolution provided by DNS can capture subpore scale events such as interfacial readjustments [19,25], cooperative filling [26], flow of films along the solid surfaces [27], and nonmonotonic behavior of the capillary pressure [26,28,29]. Performing multiple DNS realizations for a three-dimensional heterogeneous sand pack would require solving flow governing equations for a huge number of cells subsequently increasing the computational costs. Therefore, we simulate flow in two-dimensional cross-sections. The analysis presented in this study assists us to relate the large-scale features of invasion patterns and displacement efficiency to the pore-scale mechanisms controlling it. Our simulations capture the different displacement regimes (VF, CD, and VF/CD) showing that the threshold M for the crossover between the regimes increases with the wettability. VF/CD refers to the intermediate flow regime that has traits of both VF and CD which has not been captured in the earlier works of Refs. [21,23,24]. We also establish the dependence of the dominant pore filling mechanisms on the combination of M and wettability. We notice that the impact of M, θ on multiphase flows are scale dependent. That is, at the sample (macroscopic) scale—only for $M \approx 1$ (VF/CD), the displacement morphology is dependent on θ whereas, at the pore scale—an increase in the differences of the invasion protocols with the wettability become more evident as M decreases. In particular, we show that for imbibition at a given contact angle, the effective wettability changes with viscosity: from neutral-wetting (cooperative filling) to strongly wetting (film flow) with decreasing M. This further indicates that in addition to contact angle, pore geometry [17], flow conditions [30,31], the effective wettability is also a function of the viscosity ratio.

II. MATHEMATICAL MODEL

A. Governing equations

In DNS, the isothermal flow dynamics of immiscible and incompressible multiphase flow systems are governed by the Navier-Stokes equations, solved for each fluid phase, where the

fluid-fluid interfaces boundary conditions that ensure continuity in the velocity field are set. The stress gradients can be computed via the Young-Laplace equation [32]. Though this approach provides the interface dynamics, it is computationally demanding as it requires solving for a complex moving boundary problem. The volume of fluid (VOF) method simplifies the computations by considering the two fluid phases as a single mixture [33]. This is done by defining a color function $\alpha \in [0, 1]$ which indicates the volume occupied by a specific fluid in a control volume: when α is equal to 0 or 1 the volume is occupied by a single phase, whereas $1 > \alpha > 0$ indicates the co-existence of two fluids separated by at least one fluid-fluid interface. VOF then solves for conservation of both mass

$$\mathbf{\nabla} \cdot \mathbf{U} = 0 \tag{1}$$

and momentum

$$\frac{\partial(\rho \mathbf{U})}{\partial t} + \mathbf{\nabla} \cdot (\rho \mathbf{U} \mathbf{U}) = -\mathbf{\nabla} p + \mathbf{\nabla} \cdot \mu(\mathbf{\nabla} \mathbf{U} + \mathbf{\nabla} \mathbf{U}^T) + \mathbf{F}_b + \mathbf{F}_c. \tag{2}$$

In Eqs. (1) and (2), $\mathbf{U}$ is the velocity, t is time, p is pressure, $\mathbf{F}_b$ and $\mathbf{F}_c$ are the external body (for example, gravity) and capillary forces, respectively. Superscript T denotes a transpose. Considering a single mixture, its properties are assumed to be a linear combination of the two fluids comprising it; for example, denoting the wetting phase by $\alpha = 1$, the density ρ and the dynamic viscosity μ of the mixture are

$$\rho = \rho_w \alpha + \rho_n (1 - \alpha),$$
$$\mu = \mu_w \alpha + \mu_n (1 - \alpha). \tag{3}$$

The capillary forces are

$$\mathbf{F}_c = \sigma k \mathbf{n}_I \delta_I, \tag{4}$$

where σ is the surface tension, k is the interface curvature, $\mathbf{n}_I$ is the unit normal to the interface, and δ_I is a Dirac δ function, which is used to restrict the capillary forces to act only at the interface. Various VOF formulations can be used to define how the normal to the interface $\mathbf{n}_I$ and the Dirac delta function δ_I are discretized; see Pavuluri *et al.* [34]. In this work we use the conventional continuum surface force (CSF) formulation [35], in which $\mathbf{n}_I \delta_I$ from Eq. (4) are approximated by the gradient of the color function $\mathbf{\nabla} \alpha$, providing

$$\mathbf{F}_c^{\text{CSF}} = \sigma k \mathbf{\nabla} \alpha. \tag{5}$$

The interface curvature k is computed as

$$k = -\mathbf{\nabla} \cdot \mathbf{n}_I = -\mathbf{\nabla} \cdot \frac{\mathbf{\nabla} \alpha}{|\mathbf{\nabla} \alpha|}. \tag{6}$$

Closure to the system of equations is provided by the following advection equation for the color function:

$$\frac{\partial \alpha}{\partial t} + \mathbf{\nabla} \cdot (\mathbf{U} \alpha) = 0. \tag{7}$$

B. Numerical implementation

We use the VOF method implemented in OpenFOAM [36] with the interFoam solver, where the domain is discretized in space using the finite volume method, using an Eulerian mesh. The field variables such as velocity $\mathbf{U}$, pressure p and color function α are stored at the cell centers. Time is discretized by first order Euler scheme. The gradient terms are discretized using Gauss linear scheme, of second order accuracy. The advection term in the Navier-Stokes equation [second term in the left-hand side of Eq. (2)] is solved using the limited linear difference scheme. As the color function is required to be bounded, vanLeer scheme [37] is used for the advection of the color function in Eq. (7). As many other numerical schemes, VOF suffers from numerical diffusion

and smearing of interfaces, that arises from solving the discretized advection equation of the color function. To reduce this numerical artefact, an additional term $\alpha(1 - \alpha)\mathbf{U}_r$ is added to Eq. (7), where the so-called compression velocity is approximated as $\mathbf{U}_r = \min[c_\alpha \mathbf{U}_{cv}, \max(\mathbf{U}_d)]$ [38]. c_α is the compression coefficient set to one based on the studies of Deshpande *et al.* [39], Hoang *et al.* [40], Ferrari and Lunati [41], $\mathbf{U}_{cv}$ refers to the velocity in a specific control volume and $\max(\mathbf{U}_d)$ refers to the maximum velocity in the entire porous medium. The term $\alpha(1 - \alpha)$ restricts the compression velocity to act only at the interfaces.

The pressure-velocity coupling in the Navier-Stokes equations are solved using the pressure implicit with splitting of operators (PISO) algorithm [42]. To generate the discretized pore space for the simulations, we first use a rectangular mesh with cell size of $\Delta x = \Delta y = 13.5\,\mu\mathrm{m}$, and then remeshed using the snappyHexMesh library of OpenFOAM. The time step size is chosen based on the Brackbill number $t_{Bk} = \sqrt{\rho_{avg}\Delta x^3/(\pi\sigma)}$ where ρ_{avg} is the average density of fluids in the domain and $\Delta x = 13.5\,\mu\mathrm{m}$ is the cell size [35]. To reduce computational runtime, we set the time step size $\Delta t \approx 3t_{Bk}$, which for our settings provides $\Delta t = 10\,\mu\mathrm{s}$. The parameters describing the physical properties are provided in Sec. II C.

Random velocities larger in magnitude compared to the physical flows occur along the interfaces while numerically solving equations in Sec. II A which are referred to as spurious currents. Decades of research to reduce spurious currents have given rise to several VOF formulations [35,40,43–45]. Promising is the piecewise linear interface calculation (PLIC) formulation that almost entirely eliminates spurious currents [34,44]; however, the formulation is computationally expensive and current open-source solvers can only handle flows with Cartesian meshes [44]. Other popular VOF formulations are the filtered surface force (FSF)—captures the capillary fluxes and filters them, the sharp surface force (SSF)—sharpen the interfacial region thereby restricting the region where interfacial forces act [45]. FSF and SSF consider choosing several heuristic parameters which can be case dependent [34]. In pursuit to reduce spurious currents random choice of heuristic parameters could potentially alter the actual flows [26]. Therefore, for this work we chose to use the conventional CSF formulation though spurious currents exist. The use of a fine mesh accompanied by smaller time steps (according to t_{Bk}) in this study assists in reducing the impact of spurious currents as these velocities appear in a random manner and are not continuously focused at specific control volumes while solving Eq. (7). Hence, we believe that spurious currents do not play a substantial role in altering the actual flow physics in this study.

C. Settings and parameter values

We simulate displacement in a geologically realistic medium, obtained from a 2D cross section of micro-CT image of a sand pack [46] shown in Fig. 1. The sample has a porosity of $\phi = 27.8\%$ and dimensions are 6.75 and 14.05 mm in the X and Y direction. Figures SM1 and SM2 in the Supplemental Material [47] show the segmented pores and pore size distribution, respectively, for the porous medium shown in Fig. 1. In this work, we do not explicitly segregate the pore throats and pore bodies and refer to the overall pore spaces as pores. From the pore size distribution, there exists a total of 272 pores of which relatively large number of pores have pore diameter in the range 100–300 μm. While our 2D model geometry can represent subpore pore filling mechanisms in the X-Y plane, such as film flow along solid grain surfaces (filling the entire gap thickness in the Z direction), it cannot represent flows in the out-of-plane (Z) direction, where only part of the gap is filled. Thus, our model excludes corner flows [48,49] and wetting layer formation along the top and bottom plates. These mechanisms become important for the invasion of strongly wetting fluid ("strong imbibition") and strongly nonwetting fluids ("strong drainage," at high Ca) at $M \ll 1$ [15,21]. The porous medium model is discretized into 145 000 cells using the snappyHexMesh library of OpenFOAM. The zoom-in [Fig. 1(b)] shows the intricate nature of the geological media, with highly nonuniform pore bodies and throats, and dead ends. The mesh contains both Cartesian and non-Cartesian cells; non-Cartesian cells are used close to the boundaries with the solid grains, to capture the orientation of the pore spaces.
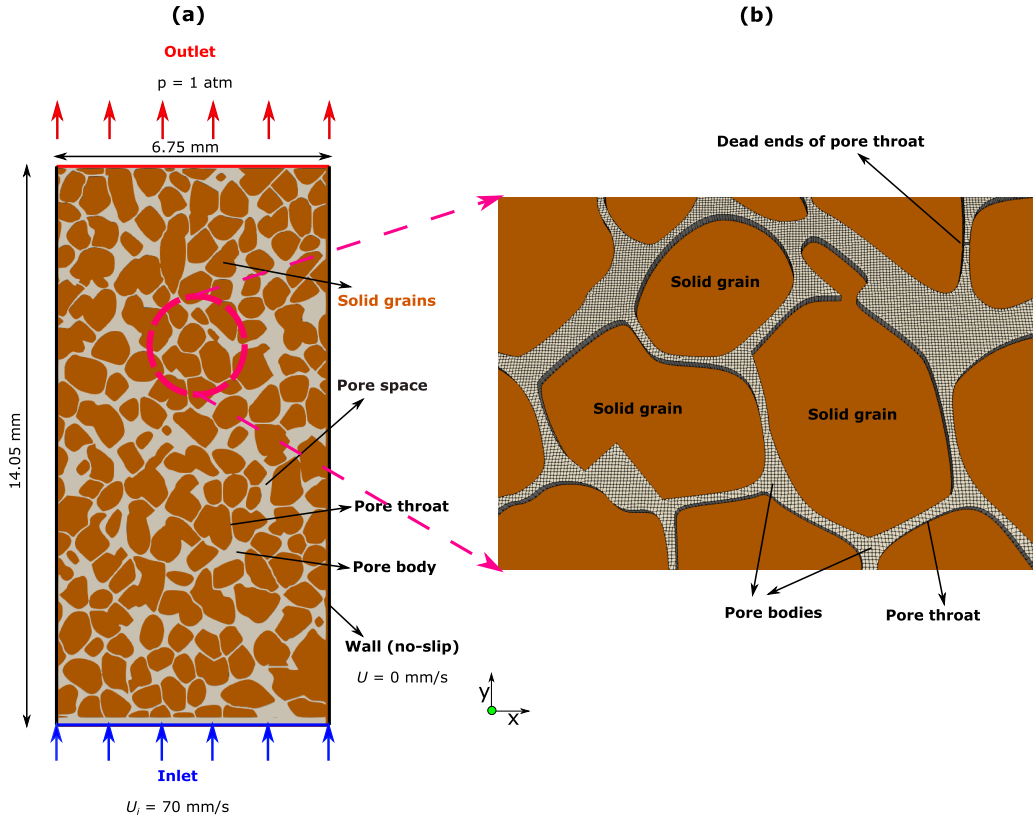
(a)

(b)

FIG. 1. (a) The simulated two-dimensional porous medium. The pore space and solid grains are shown in gray and brown, respectively, (b) zoom-in showing the meshed pore space.

The boundary conditions are, fixed injection velocity of the invading fluid at the inlet face at $U_i = 70$ mm/s, fixed pressure $p = 1$ atm at the outlet, and no-flow at the other two (lateral) boundaries [Fig. 1(a)]. The surfaces of solid grains are subjected to no-slip boundary conditions. The interface normal $\mathbf{n}_I$ pointing towards the invading phase orients the interface according to $\mathbf{n}_I = \mathbf{n}_W \cos(\theta) + \mathbf{t}_W \sin(\theta)$, where $\mathbf{n}_W$ is the normal to the solid grain surfaces, $\mathbf{t}_W$ is the tangent to the solid grain surfaces and θ is the equilibrium contact angle that the injected phase makes with the solid surfaces [35]. While we specify the equilibrium contact angle for the simulations, a combination of parameters such as the fluid velocity and the orientation of the pore spaces results in an effective wettability.

We vary the contact angle in the range of $\theta \in [0°, 180°]$ with $\theta = 20°$ increments. Imbibition and drainage refer to $\theta < 90°$ and $\theta > 90°$, respectively. At $\theta = 0°$ ("strong imbibition"), the injected fluid perfectly wets the solid surfaces. At $\theta = 180°$ ("strong drainage"), the injected fluid is perfectly nonwetting, such that it repels from the solid surfaces. The viscosity ratio, $M = \mu_i/\mu_d$, was varied between 0.01 and 100, by setting the maximum viscosity of one fluid to $\mu_{max} = 0.1$ kg/ms and tuning the viscosity of the other. Here μ_i and μ_d are the viscosities of the invading and defending fluids, respectively. We set the density of both fluids to $\rho = \rho_i = \rho_d = 1000$ kg/m³, and the surface tension to $\sigma = 0.07$ kg/s². The capillary number, defined here as $\text{Ca} = U_i \mu_{max}/\sigma$ was fixed at 10^{-3}. We chose this Ca value to focus on viscous-dominated flow versus the capillary-dominated flow at $\text{Ca} \leqslant 1 \times 10^{-4}$ investigated elsewhere [11,50,51]. The total number of simulations were 90: 10 values of θ and 9 values of M. Simulations were run using

parallel computations with 16 Intel Xeon E5-2690 processors (clock speed 2.60 GHz). With that, simulating 1 physical second of flow requires runtime of ∼3.5 h.

D. Image processing for quantitative analysis of patterns

Quantitative analysis of the observed patterns at breakthrough is done using two characteristics: (i) the displacement efficiency D_e, which is the volume of the displaced defending fluid normalized by the total pore volume; and (ii) the fractal dimensions D_f, an estimation of the roughness of the interface, which we compute using the box-counting method [52]. The fractal dimensions in 2D is bounded at $D_f \in [1 - 2]$, where $D_f = 1$ and $D_f = 2$ represent the highest possible roughness and a completely compact interfacial morphology, respectively. These computations are done on a binary format (white for the injected fluid, black for everything else). Conversion of the invasion images into binary format was done using Fiji software [53]. Supplemental Material [47] provides a brief description regarding the procedure followed to determine D_f in Fiji.

III. RESULTS

A. Displacement patterns

We begin with a qualitative analysis based on the visual appearance of the patterns, followed by quantitative characterization using fractal dimension. Figure 2 shows the simulated patterns at breakthrough for the 90 conditions (varying independently M and θ) considered here. The displacement patterns change from viscous fingering (VF) to compact displacement (CD), with an intermediate regime (VF/CD) exhibiting a mix of features from both. VF, characterized by long and narrow fingers, emerges at $M \leqslant 0.01$ irrespective of θ. The fluid fingers in imbibition are slightly wider compared to those in drainage, also observed in Ref. [23]. This is due to the increased tendency of the invading fluid to minimize contact with the solid surfaces in drainage. VF was also observed in Ref. [21], however at $M < 0.5$. At $M \geqslant 10$, the invading fluid fills most of the pore space leading to CD, again irrespective of θ. At intermediate values of $M \approx 1$, a transition between VF and CD occurs; the M value for the transition among the regimes depends on θ. From Fig. 2 it can be seen that θ has relatively more influence on the fluid displacement patterns at $M \approx 1$ compared to when M is substantially low or high.

Figure SM3 in the Supplemental Material [47] provides a complementary figure showcasing the displacement patterns (for all 90 cases investigated) highlighting the solids, invading and defending fluids for reference. Additionally, three videos of the invasion processes occurring at $\theta = 60°$ for $M = 0.01$ (VF, Video 1), 1 (VF/CD, Video 2), and 100 (CD, Video 3) are also provided in the Supplemental Material. For $M = 1, \theta = 60°$ (Video 2), the flow regime VF/CD shows traits of CD—starting from the inlet boundary extending upto a certain length of the porous medium ℓ_{CD}, VF—extending from the tip of ℓ_{CD} until the outlet boundary. Similar sort of flow behavior was experimentally observed by [54] while investigating the transition from VF to CD by varying M, Ca and keeping θ fixed. In our study, we notice ℓ_{CD} to reduce with increasing θ for a constant M. Refer to Video 2 of the Supplemental Material [47] to notice the initial development of the fingers along the sides of the porous medium that gradually develop over time. In parallel, the pore space in-between the developed fingers gradually get invaded resembling CD.

Next, we analyze the patterns quantitatively, using (a) the displacement efficiency D_e and (b) the fractal dimensions D_f. Figure SM4 in the Supplemental Material [47] showcases results of D_e, D_f for the 90 cases investigated in this study. The more compact, less preferential invasion is characterized by larger D_e and D_f (Fig. 3). Consequently, as the invading fluid becomes more wetting, i.e., as θ decreases, both D_e and D_f increase, in most cases regardless of M. Similarly, for a given θ, increasing M stabilizes the displacement thus increasing D_e and D_f. The efficiency increases from $D_e < 30\%$ at $M = 0.01$ and $\theta = 180°$ (drainage at nonfavorable viscosity ratio, VF) to $D_e > 80\%$ at $M = 100$ and $\theta = 0°$ (imbibition at favorable viscosities, CD).

Combining the qualitative classification of the 90 simulated patterns (based on visual appearance, cf. Fig. 2) with their D_f values, allows us to establish the corresponding range of D_f values for
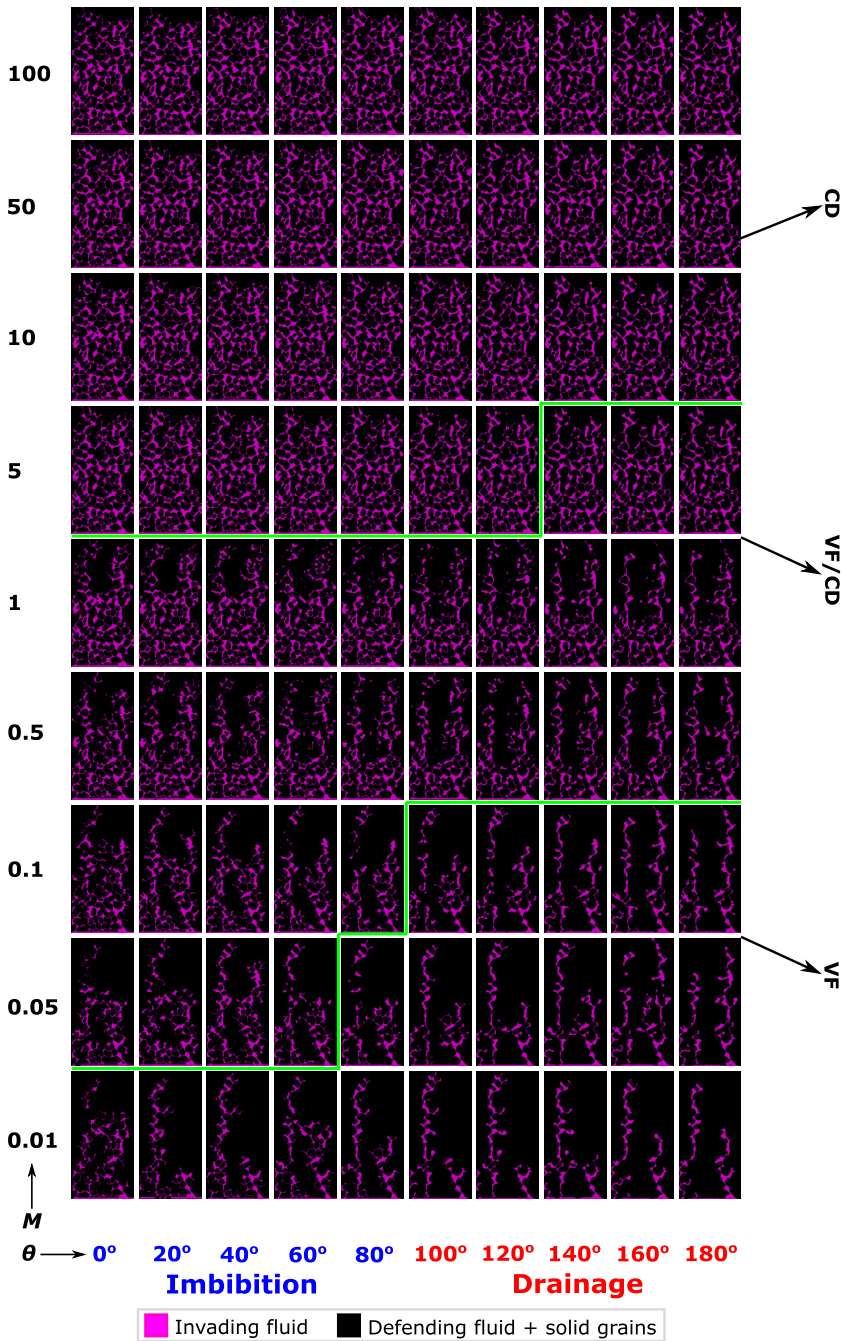
FIG. 2. Fluid displacement patterns for different contact angles θ and viscosity ratios M. The invading fluid is shown in pink, defending fluid and the solid grains are shown in black. The continuous green lines indicate transition between flow regimes: viscous fingering (VF) to intermediate (VF/CD) and intermediate to compact (CD).
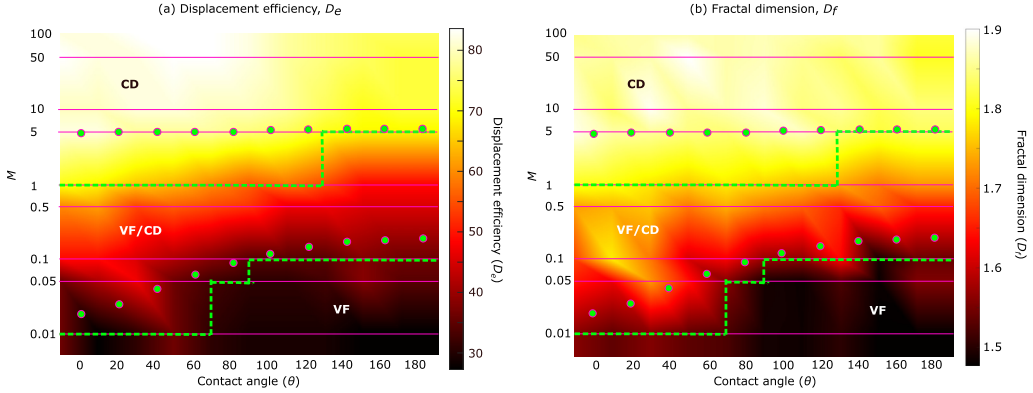
FIG. 3. Phase diagram of displacement patterns classified based on (a) D_e, (b) D_f, as a function of viscosity ratio M (represented on $\log_{10}$ scale) and wettability θ. Results of D_e, D_f from simulations (90 combinations of M and θ) are linearly interpolated. Dashed green lines indicate boundaries between regimes based on visual observations and D_f. The green dots indicate theoretical phase boundaries estimated through stability analysis.

each regime: $D_f < 1.6$ for VF, $D_f = 1.6$–1.83 for intermediate (VF/CD) regime, and $D_f > 1.83$ for CD; our D_f values agree well with published values for these regimes [55]. Plotting D_e, D_f in the form of a phase diagram, provides a quantitative estimation of the phase boundaries between regimes (dashed green line in Fig. 3). These phase boundaries (dashed green line) agree well with theoretical values obtained using the classical stability analysis by Saffman and Taylor [56] (plotted as green dots in Fig. 3); for derivation details see the Appendix. The value of M at the boundary between regimes increases with θ, in particular for the crossover between VF and VF/CD (Fig. 3). Refer to the Supplemental Material [47] where we comment on the impact of domain size on the observations reported in this section.

B. Pore filling mechanisms

The pore-scale mechanisms, controlling the manner by which pores are filled, eventually dictate the larger, sample (macroscopic) scale patterns. Valuable information about these mechanisms is obtained here by analyzing the effective pore size distribution (PSD$_e$) of the invaded pores. Figure SM8 in the Supplemental Material [47] shows the PSD$_e$ of the invaded pores for five different M at $\theta = 0°$, $80°$, $180°$ determined using the distance transform watershed method [57]. Supplemental Material [47] briefly explains the protocol followed to obtain the PSD$_e$ shown in Fig. 4. As the trends related to the frequency of pores occupied by the invading fluid at different M are representative, for the sake of brevity we show results for three values of $M = 0.01, 1, 100$ in Fig. 4.
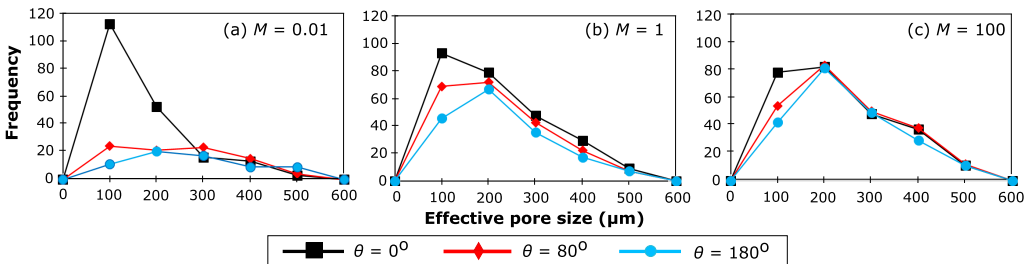

FIG. 4. Effective pore size distribution of the invading fluid for (a) $M = 0.01$ (VF), (b) $M = 1$ (VF/CD), and (c) $M = 100$ (CD) at $\theta = 0°$, $80°$, $180°$.

We use the term effective pore size in this context as a single pore (obtained through pore segmentation in Fig. SM2) could comprise frequencies (segments of the pore spaces occupied by the invading fluid) of one or greater as shown in Fig. SM7 of the Supplemental Material [47]. This is because, the frequencies of the invading fluid computed using the algorithm are dependent on the invading fluids displacement morphology (displacement occurring through narrow/wider pores) and also the presence of ganglions of the invading/defending fluid that form due to the ongoing flow dynamics in the porous medium.

Figure 4 demonstrates the strong effect of wettability at small (unstable) viscosity ratio, $M = 0.01$ [VF; Fig. 4(a)]. In contrast, it shows the small effect of θ in stable, compact displacement, with $M = 100$ [CD; Fig. 4(c)]. It is also interesting to examine the PSD_e symmetry: the invaded PSD_e is relatively symmetric (and uniform) for $M = 100$, slightly skewed for $M = 1$, and strongly skewed for $M = 0.01$ at strong imbibition ($\theta = 0°$) (Fig. 4). To explain this, we further analyze the pore filling mechanisms during individual invasion events.

We investigate the pore filling mechanisms in a small region composed of a few pores both qualitatively (visually) and quantitatively through the evolution of the local capillary pressure p_c. The local capillary pressure, $p_c = p_n - p_w$ where p_n and p_w are the volume-average nonwetting and wetting phase pressure, respectively, is computed as $p_i = \frac{\sum p_i V_c}{\sum V_c}$ where $i \in (w, n)$ and V_c is the volumes of the computational cells within the analyzed region. We track the evolution of the local pressure p_c versus the local wetting phase saturation S_w^*. The latter is normalized by the maximum S_w attained as the invading fluid reaches breakthrough on all four boundaries of the observation window (red rectangle in Fig. 5). Through visual observations we notice that during imbibition pores are filled primarily by two mechanisms: (i) film flow and (ii) cooperative filling, depending on the viscosities (Fig. 5). We briefly describe the events below and an elaborate explanation about the filling mechanisms can be found in the Supplemental Material [47]. At $M = 0.01$ (VF), the wetting phase advances as thin films coating the solid surfaces [15] [Fig. 5(b)]. With this mechanism, the
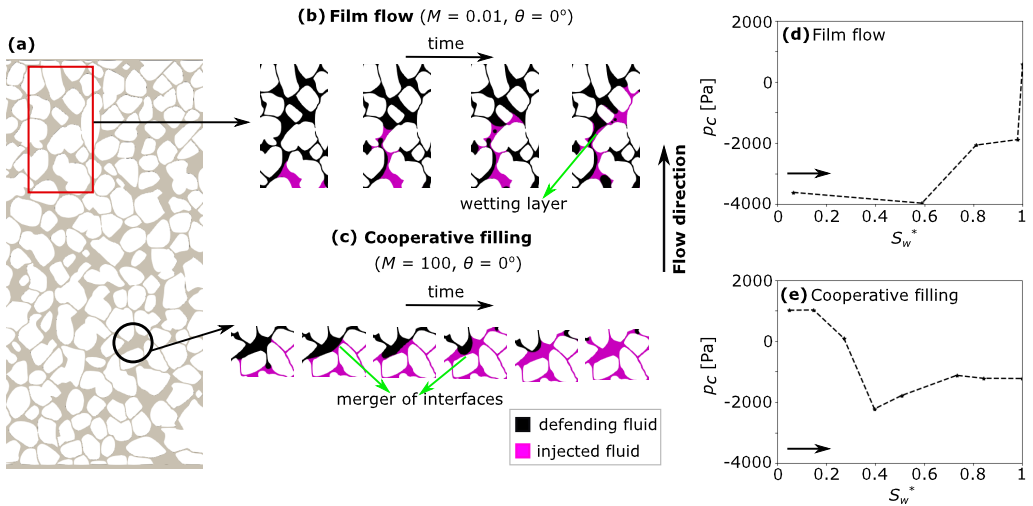

FIG. 5. Pore filling mechanisms in strong imbibition ($\theta = 0°$). Focusing on small region containing several pores [red rectangle in panel (a)], progression of invasion is shown as successive snapshots (injected fluid in pink, defending fluids in black and solid in white), for unfavorable and favorable M, 0.01 and 100, respectively [panels (b) and (c)]. At $M = 0.01$, the injected fluid propagates in the form of wetting layers that coat the solid surfaces (green arrow), invades smaller pores (b). At $M = 100$, cooperative filling (green arrows) is the dominant mechanism, leading to more uniform invasion of both small and large pore (c). Panels (d) and (e) show the evolution of the local capillary pressure with saturation of wetting fluid (S_w^*) for the two mechanisms (arrows indicate direction of change in S_w^* with time).

invasion progresses predominantly through smaller pores, in accordance with the PSD_e analysis [Fig. 4(a)]. The evolution of p_c shows a decrease in p_c magnitude upon imbibition (i.e., increasing S_w^*), see Fig. 5(d), which can be due to the formation of wetting layers that eventually results in the formation of smaller interfacial curvatures $p_c \propto k$. At moderately high M of 1–100, cooperative filling becomes the dominant mechanism [Fig. 5(c)], resulting in a more stable, compact front. During cooperative filling, multiple meniscus merge together to form a single meniscus favoring the invasion of large pore spaces. This mechanism fills the various pore sizes more uniformly than at $M = 0.01$, as can be seen by comparing the PSD_e of filled pores in Fig. 4(c) (moderately high M) versus Fig. 4(a) ($M = 0.01$). The local capillary pressure p_c drops [by $\sim$1000 Pa, Fig. 5(e)] until $S_w^* \approx 0.3$ as the invading fluid reaches the entrances of the pore body. As the invasion continues, several interfaces merge which increases p_c at $S_w^* = 0.4$. Following that, cooperative filling continues and p_c reaches a steady value as the average menisci curvature during these events does not change significantly.

For strong drainage ($\theta = 180°$), the two dominant pore filling mechanisms visually observed are (i) intermittent local jumps ("bursts") and (ii) cooperative filling (Fig. 6). We briefly describe the events below and refer to the Supplemental Material [47] for elaborate discussion about the events. At $M = 0.01$, the pores are filled by a sequence of localized bursts, leading to VF [Fig. 6(b)]. As in this regime viscous forces dominate over capillary forces, the location of invasion depends more on the global pressure gradients controlled by pore connectivity and less on the local pore sizes. Therefore, we often noticed drainage through a combination of narrower and wider pore spaces (narrower pore spaces are considered to be unfavourable during drainage) though there exist interfaces connected to wider pore spaces. This is why the PSD_e in this case is relatively uniform [Fig. 4(a)]. The local pressure p_c decreases as drainage progresses [decrease in S_w^*;
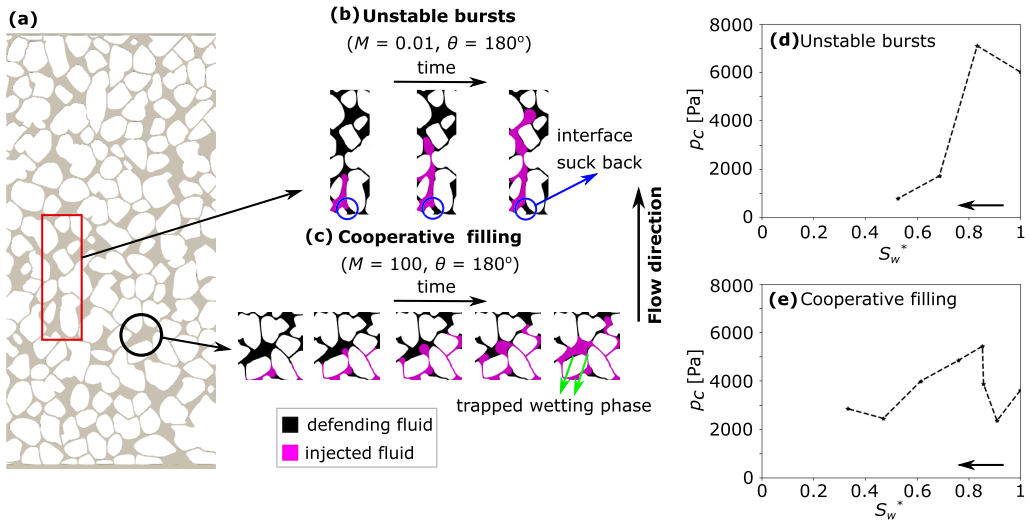

FIG. 6. Pore filling mechanisms in strong drainage ($\theta = 180°$). Focusing on small region containing several pores [panel (a)], progression of invasion is shown as successive snapshots (injected fluid in pink, defending fluids in black and solid in white), for unfavorable and favorable M, 0.01 and 100, respectively [panels (b) and (c)]. At $M = 0.01$, the injected fluid propagates by a sequence of unstable bursts, which also involve interfacial readjustments [blue arrow, panel (b)]. At $M = 100$, cooperative filling (green arrows) is the dominant mechanism; however, unlike in imbibition, as the invading fluid is nonwetting here it leaves small pockets of trapped defending fluid [green arrows; panel (c)]. Both mechanisms lead to relatively uniform invasion in terms of pore sizes. Panels (d) and (e) show the evolution of the local capillary pressure with saturation of wetting fluid (S_w^*) for the two mechanism (arrows indicate direction of change in S_w^* with time).

Fig. 6(d)]. This can be explained due to the formation of menisci that remain stagnant due to interfacial readjustments and the evolution of the curvatures of the invading fluid front. As M increases, cooperative filling becomes dominant, making the displacement pattern more compact [Fig. 6(d)], and increasing the uniformity of invaded pore sizes [Fig. 4(c)]. While the mechanism seems similar to that in imbibition at high M, in drainage as the invading fluid is less wetting it does not completely displace the defending (wetting) fluid which remains trapped in small pockets [Fig. 6(c)]. Unlike cooperative filling in imbibition where $p_c \approx 0$ as the interfaces reach entrance to the pore body, in drainage the tendency of the invading fluid to repel from the solid surfaces and invade mainly the larger pores results in maintaining a finite interfacial curvature at all times (versus $p_c \approx 0$ in imbibition), cf. Fig. 6(e). Here, p_c decreases as the invading fluid fills the pore bodies ($S_w^* = 0.8$–0.5), with a very moderate rise after interfaces merge.

The presented analysis of pore filling mechanisms provides an interesting link between the effective wettability conditions and the viscosities, M. Published simulations and experiments observed cooperative filling at intermediate wet conditions [15,58,59]. Our simulations suggest that M changes the effective wettability, and thus the dominant mechanism: from cooperative filling at moderate and high M to film flow (during imbibition) and bursts (during drainage) at low M.

Though not part of this study, we elaborate in the Supplemental Material [47] how considering a 3D setup and scaled domain size impacts the quantitative results presented above.

IV. SUMMARY AND CONCLUSIONS

We leverage high-resolution direct numerical simulation (DNS) to uncover the synergistic impact of wettability and viscous forces in viscous-dominated multiphase flow through a heterogeneous geologically realistic porous media. We present a phase diagram classifying invasion patterns into viscous fingering (VF), compact displacement (CD), and intermediate regime (CD/VF), with a transition from compact upstream to VF downstream. At the macroscopic (sample) scale, the wettability of porous media plays a pivotal role in controlling the crossover between regimes. Our simulations indicate an increase in threshold M (at which the crossover between regimes occurs) as wetting properties vary from imbibition to drainage. Wettability was also found to affect the pore filling mechanisms. For low M (VF), film flow dominated during imbibition and bursts during drainage. This strong effect of wettability over the pore-filling behavior diminishes as M increases: cooperative filling was found to be dominating in CD irrespective of wettability. Using pore filling mechanism as an indicator of effective wettability [58] we can deduce from Figs. 5 and 6 that the change in mechanism from cooperative filling to film flow as the M decreases manifests a change in effective wettability conditions from neutral-wet to strong-wet, respectively. Furthermore, the analysis presented showcases that the impact of M, θ on multiphase flows is scale-dependent as wettability is seen to play a role in the displacement patterns at $M \approx 1$ at the sample scale whereas, at the pore-scale the effect of wettability was observed to be significant at low M. These intriguing effects of viscosity on effective wettability should be considered in modeling multiphase fluids of similar viscosities, which is of interest to applications such as nonaqueous phase liquid (NAPLs) contamination and enhanced hydrocarbon recovery.

APPENDIX: DERIVATIONS OF PHASE BOUNDARY FROM LINEAR STABILITY ANALYSIS

Here we describe the evaluation of the theoretical phase boundaries (green dots in Fig. 3) using the linear stability analysis by Saffman and Taylor [56]. Considering the relation between fluid flow

potential φ and fluid velocity as $\mathbf{U} = \nabla\varphi$, the continuity equation Eq. (1) for each individual phase i can be written as

$$\nabla \cdot \nabla\varphi_i = \nabla^2\varphi_i = 0. \tag{A1}$$

With this, force balance becomes [56]

$$\left[\mathbf{U}\epsilon - \frac{\alpha\epsilon}{\gamma}\right]\frac{\mu_d}{k_d} - \left[\mathbf{U}\epsilon + \frac{\alpha\epsilon}{\gamma}\right]\frac{\mu_i}{k_i} = \frac{2\sigma\cos(\theta)}{r}, \tag{A2}$$

where ϵ represents the location of the perturbed displacement (finger) front relative to the base state—the interface morphology before fingers develop. Here, α is the growth rate of the perturbations and γ is the wave number indicating the number of periodic disturbances in the developed finger (see further details in Saffman and Taylor [56], Rabbani *et al.* [60]). The stability analysis proposed by Saffman and Taylor [56] considered $b^2/12$ (b being the width between two parallel plates in a Hele-Shaw cell) to be the permeability $k = k_i = k_d$. However for our case, due to the presence of solid grains in the system and as the presence of the defending fluid impacts the displacement of the injected phase, the effective permeability k_α is considered to be a function of the pore geometry and the fluid saturation. Therefore, the effective permeability of the injected fluid can be approximated as $k_i = 2\phi\lambda r\epsilon/n$ where r is the pore radius, n are the total number of pores in the considered porous medium [60]. $n = 272$ are the total number of pores in the porous medium obtained through pore size distribution study. λ in the expression for k_i is determined empirically to be $\lambda = \overline{D_e}n_f[l_f w_f/lw][w_f/w]$. The product $l_f w_f$ is the approximate area occupied by a single finger, where l_f and w_f are the length and width of the finger, respectively. We assume $w_f = 1$ mm and $l_f = l_p\tau$ where l_p is the length of the porous media over which the fingers develop and τ is the effect of tortuosity [61]. For VF, as the fingers are of the size of the entire domain length, we use $l_p = 14.05$ mm. For VF/CD, as the fingers roughly exist over half the length of the porous medium, we use $l_p = 7$ mm. To account for the effect of tortuosity, we use $l_f = 1.5l_p$. For VF, $l_f \approx 20$ mm and for VF/CD, $l_f \approx 10$ mm. We normalize $l_f w_f$ by the area lw (medium dimensions). $n_f = 2$ refers to the number of fingers formed in general. $\overline{D_e}w_f/w$ is an empirical parameter used to determine λ such that M in Eq. (A4) does not become negative. We obtain $\overline{D_e} \approx 32.5\%$ for VF, $\overline{D_e} \approx 65\%$ for VF/CD are the average displacement efficiencies. Assuming a proportionality between the effective permeabilities of the two fluids $k_d = Ak_i$ [62], we manipulate Eq. (A2) to obtain

$$-\frac{\alpha}{\gamma}\left[\frac{1}{A} + M\right] + \mathbf{U}\left[\frac{1}{A} - M\right] = \frac{4\sigma\cos(\theta)\phi\lambda}{\mu_d n}. \tag{A3}$$

The crossover between flow regimes is expected to occur when $\alpha = 0$ [60]. Substituting $\alpha = 0$ in Eq. (A3) provides the following condition:

$$M = \frac{1}{A} - \frac{4\phi\lambda\cos(\theta)}{\mathrm{Ca}n}. \tag{A4}$$

In the above equation, A is determined empirically. For VF, the invading fluid propagates through the porous medium in the form of thin fingers. Therefore, most of the pores remain occupied by the defending fluid. As the effective permeabilities k_i are function of phase saturation S_i [62], this imply that the transition from VF to VF/CD occurs at $A = k_d(S_d)/k_i(S_i) > 1$. For this case, we assume $A = \frac{1}{D_e\phi} \approx 10$. While considering VF/CD to CD, more than half of the porous medium is occupied by the invading fluid essentially making $A < 1$. For this case, we assume $A = \overline{D_e}\phi \approx 0.2$. Substituting all the above variables in Eq. (A4) gives the threshold viscosity ratio (the boundary between regimes) at which transition between flow regimes occur indicated by green circles in Fig. 3. We note that the threshold M increases with θ, in particular for the crossover between VF and VF/CD (Fig. 3). Interestingly, for the idealized geometry in Primkulov *et al.* [21] the transition from VF to CD occurred at $M \approx 0.5$ irrespective of the wettability, without an intermediate VF/CD regime which could potentially be due to the relatively simplistic nature of the models used in PNM.

[1] B. Metz, O. Davidson, H. De Coninck, M. Loos, and L. Meyer, *IPCC Special Report on Carbon Dioxide Capture and Storage* (Cambridge University Press, Cambridge, UK, 2005)

[2] M. E. Boot-Handford, J. C. Abanades, E. J. Anthony, M. J. Blunt, S. Brandani, N. Mac Dowell, J. R. Fernández, M.-C. Ferrari, R. Gross, J. P. Hallett *et al.*, Carbon capture and storage update, Energy Environ. Sci. **7**, 130 (2014).

[3] J. F. Villaume, Investigations at sites contaminated with dense, nonaqueous phase liquids (NAPLs), Groundwater Monit. Rem. **5**, 60 (1985).

[4] A. S. Mayer, *Soil and Groundwater Contamination: Nonaqueous Phase Liquids*, Water Resources Monograph Series, Vol. 17 (American Geophysical Union, Washington, D.C., 2005).

[5] D. M. Mackay and J. A. Cherry, Groundwater contamination: Pump-and-treat remediation, Environ. Sci. Technol. **23**, 630 (1989).

[6] M. J. O'Sullivan, K. Pruess, and M. J. Lippmann, State of the art of geothermal reservoir simulation, Geothermics **30**, 395 (2001).

[7] E. Barbier, Geothermal energy technology and current status: An overview, Renew. Sustain. Energy Rev. **6**, 3 (2002).

[8] J. J. Sheng, *Modern Chemical Enhanced Oil Recovery: Theory and Practice* (Gulf Professional Publishing, Houston, TX, 2010).

[9] T. Cyr, R. Coates, and M. Polikar, Steam-assisted gravity drainage heavy oil recovery process (2001), U.S. Patent No. 6,257,334.

[10] D. Avraam and A. Payatakes, Flow regimes and relative permeabilities during steady-state two-phase flow in porous media, J. Fluid Mech. **293**, 207 (1995).

[11] R. Lenormand, E. Touboul, and C. Zarcone, Numerical models and experiments on immiscible displacements in porous media, J. Fluid Mech. **189**, 165 (1988).

[12] R. Lenormand, Liquids in porous media, J. Phys.: Condens. Matter **2**, SA79 (1990).

[13] M. Trojer, M. L. Szulczewski, and R. Juanes, Stabilizing Fluid-Fluid Displacements in Porous Media Through Wettability Alteration, Phys. Rev. Appl. **3**, 054008 (2015).

[14] R. Holtzman and E. Segre, Wettability Stabilizes Fluid Invasion into Porous Media via Nonlocal, Cooperative Pore Filling, Phys. Rev. Lett. **115**, 164501 (2015).

[15] B. Zhao, C. W. MacMinn, and R. Juanes, Wettability control on multiphase flow in patterned microfluidics, Proc. Natl. Acad. Sci. USA **113**, 10251 (2016).

[16] H. S. Rabbani, V. Joekar-Niasar, T. Pak, and N. Shokri, New insights on the complex dynamics of two-phase flow in porous media under intermediate-wet conditions, Sci. Rep. **7**, 4584 (2017).

[17] H. S. Rabbani, B. Zhao, R. Juanes, and N. Shokri, Pore geometry control of apparent wetting in porous media, Sci. Rep. **8**, 15729 (2018).

[18] R. Hu, J. Wan, Z. Yang, Y.-F. Chen, and T. Tokunaga, Wettability and flow rate impacts on immiscible displacement: A theoretical model, Geophys. Res. Lett. **45**, 3077 (2018).

[19] S. Pavuluri, J. Maes, J. Yang, M. Regaieg, A. Moncorgé, and F. Doster, Towards pore network modelling of spontaneous imbibition: Contact angle dependent invasion patterns and the occurrence of dynamic capillary barriers, Comput. Geosci. **24**, 951 (2020).

[20] T. Zakirov and M. Khramchenkov, Wettability effect on the invasion patterns during immiscible displacement in heterogeneous porous media under dynamic conditions: A numerical study, J. Pet. Sci. Eng. **206**, 109049 (2021).

[21] B. K. Primkulov, A. A. Pahlavan, X. Fu, B. Zhao, C. W. MacMinn, and R. Juanes, Wettability and Lenormand's diagram, J. Fluid Mech. **923**, A34 (2021).

[22] B. K. Primkulov, S. Talman, K. Khaleghi, A. Rangriz Shokri, R. Chalaturnyk, B. Zhao, C. W. MacMinn, and R. Juanes, Quasistatic fluid-fluid displacement in porous media: Invasion-percolation through a wetting transition, Phys. Rev. Fluids **3**, 104001 (2018).

[23] P. Mora, G. Morra, D. A. Yuen, and R. Juanes, Influence of wetting on viscous fingering via 2D Lattice Boltzmann simulations, Transp. Porous Media **138**, 511 (2021).

[24] S. Bakhshian, H. S. Rabbani, and N. Shokri, Physics-driven investigation of wettability effects on two-phase flow in natural porous media: Recent advances, new insights, and future perspectives, Transp. Porous Media **140**, 85 (2021).

[25] A. Ferrari and I. Lunati, Inertial effects during irreversible meniscus reconfiguration in angular pores, Adv. Water Resour. **74**, 1 (2014).

[26] S. Pavuluri *et al.*, Direct numerical simulations of spontaneous imbibition at the pore-scale: Impact of parasitic currents and dynamic capillary barriers, Ph.D. thesis, Heriot-Watt University, 2019.

[27] M. O. Abu-Al-Saud, A. Riaz, and H. A. Tchelepi, Multiscale level-set method for accurate modeling of immiscible two-phase flow with deposited thin films on solid surfaces, J. Comput. Phys. **333**, 297 (2017).

[28] H. S. Rabbani, V. Joekar-Niasar, and N. Shokri, Effects of intermediate wettability on entry capillary pressure in angular pores, J. Colloid Interface Sci. **473**, 34 (2016).

[29] H. S. Rabbani and T. D. Seers, Inertia controlled capillary pressure at the juncture between converging and uniform channels, Sci. Rep. **9**, 13870 (2019).

[30] O. Voinov, Hydrodynamics of wetting, Fluid Dyn. **11**, 714 (1976).

[31] R. Cox, The dynamics of the spreading of liquids on a solid surface. Part 1. Viscous flow, J. Fluid Mech. **168**, 169 (1986).

[32] G. K. Batchelor, *An Introduction to Fluid Dynamics* (Cambridge University Press, Cambridge, UK, 2000).

[33] C. W. Hirt and B. D. Nichols, Volume of fluid (VOF) method for the dynamics of free boundaries, J. Comput. Phys. **39**, 201 (1981).

[34] S. Pavuluri, J. Maes, and F. Doster, Spontaneous imbibition in a microchannel: Analytical solution and assessment of volume of fluid formulations, Microfluid. Nanofluid. **22**, 90 (2018).

[35] J. U. Brackbill, D. B. Kothe, and C. Zemach, A continuum method for modeling surface tension, J. Comput. Phys. **100**, 335 (1992).

[36] https://openfoam.org.

[37] B. van Leer, Towards the ultimate conservative difference scheme. V. A second-order sequel to Godunov's method, J. Comput. Phys. **32**, 101 (1979).

[38] H. Rusche, Computational fluid dynamics of dispersed two-phase flows at high phase fractions, Ph.D. thesis, Imperial College London, University of London, 2003.

[39] S. S. Deshpande, L. Anumolu, and M. F. Trujillo, Evaluating the performance of the two-phase flow solver interfoam, Comput. Sci. Disc. **5**, 014016 (2012).

[40] D. A. Hoang, V. van Steijn, L. M. Portela, M. T. Kreutzer, and C. R. Kleijn, Benchmark numerical simulations of segmented two-phase flows in microchannels using the volume of fluid method, Comput. Fluids **86**, 28 (2013).

[41] A. Ferrari and I. Lunati, Direct numerical simulations of interface dynamics to link capillary pressure and total surface energy, Adv. Water Resour. **57**, 19 (2013).

[42] R. I. Issa, Solution of the implicitly discretized fluid flow equations by operator-splitting, J. Comput. Phys. **62**, 40 (1986).

[43] B. Lafaurie, C. Nardone, R. Scardovelli, S. Zaleski, and G. Zanetti, Modelling merging and fragmentation in multiphase flows with surfer, J. Comput. Phys. **113**, 134 (1994).

[44] S. Popinet, An accurate adaptive solver for surface-tension-driven interfacial flows, J. Comput. Phys. **228**, 5838 (2009).

[45] A. Q. Raeini, M. J. Blunt, and B. Bijeljic, Modelling two-phase flow in porous media at the pore scale using the volume-of-fluid method, J. Comput. Phys. **231**, 5653 (2012).

[46] T. Pak, H. S. Rabbani, A. Qaseminejad Raeini, and N. Shokri, Effects of the pore morphology on multiphase fluid displacement in porous media—A high-resolution modeling investigation, ACS omega **8**, 3889 (2023).

[47] See Supplemental Material at http://link.aps.org/supplemental/10.1103/PhysRevFluids.8.094002 for the segmented pores (Fig. SM1); pore size distribution (Fig. SM2) for the considered porous medium in this study; invading, defending fluids configurations along with the solid grains at breakthrough for different viscosity ratios and contact angles (Fig. SM3); displacement efficiency and fractal dimension values from all simulations (Fig. SM4); methodology used to determine fractal dimensions (Fig. SM5); methodology to compute the effective pore size distribution of invaded phase (Figs. SM6 and SM7); results of effective pore size distribution of invaded phase for different viscosity ratios and contact angles (Fig. SM8); videos of different fluid displacement patterns (VF Video 1, VF/CD Video 2, CD Video 3); explanation about the pore filling mechanisms; impact of domain size and dimensionality on the presented results.

[48] M. J. Blunt, Flow in porous media—Pore-network models and multiphase flow, Curr. Opin. Colloid Interface Sci. **6**, 197 (2001).

[49] A. Mazouchi and G. Homsy, Thermocapillary migration of long bubbles in polygonal tubes. I. Theory, Phys. Fluids **13**, 1594 (2001).

[50] M. Ferer, C. Ji, G. S. Bromhal, J. Cook, G. Ahmadi, and D. H. Smith, Crossover from capillary fingering to viscous fingering for immiscible unstable flow: Experiment and modeling, Phys. Rev. E **70**, 016303 (2004).

[51] S. An, H. Erfani, O. E. Godinez-Brizuela, and V. Niasar, Transition from viscous fingering to capillary fingering: Application of GPU-based fully implicit dynamic pore network modeling, Water Resour. Res. **56**, e2020WR028149 (2020).

[52] J. Feder, *Fractals* (Springer Science & Business Media, Berlin, 2013).

[53] J. Schindelin, I. Arganda-Carreras, E. Frise, V. Kaynig, M. Longair, T. Pietzsch, S. Preibisch, C. Rueden, S. Saalfeld, B. Schmid *et al.*, Fiji: An open-source platform for biological-image analysis, Nat. Methods **9**, 676 (2012).

[54] F. K. Eriksen, M. Moura, M. Jankov, A. L. Turquet, and K. J. Måløy, Transition from viscous fingers to compact displacement during unstable drainage in porous media, Phys. Rev. Fluids **7**, 013901 (2022).

[55] G. Løvoll, Y. Méheust, R. Toussaint, J. Schmittbuhl, and K. J. Måløy, Growth activity during fingering in a porous Hele-Shaw cell, Phys. Rev. E **70**, 026301 (2004).

[56] P. G. Saffman and G. I. Taylor, The penetration of a fluid into a porous medium or hele-shaw cell containing a more viscous liquid, Proc. R. Soc. London A **245**, 312 (1958).

[57] D. Legland, I. Arganda-Carreras, and P. Andrey, Morpholibj: Integrated library and plugins for mathematical morphology with imagej, Bioinformatics **32**, 3532 (2016).

[58] M. Cieplak and M. O. Robbins, Dynamical Transition in Quasistatic Fluid Invasion in Porous Media, Phys. Rev. Lett. **60**, 2042 (1988).

[59] M. Cieplak and M. O. Robbins, Influence of contact angle on quasistatic fluid invasion of porous media, Phys. Rev. B **41**, 11508 (1990).

[60] H. S. Rabbani, D. Or, Y. Liu, C.-Y. Lai, N. B. Lu, S. S. Datta, H. A. Stone, and N. Shokri, Suppressing viscous fingering in structured porous media, Proc. Natl. Acad. Sci. USA **115**, 4833 (2018).

[61] W. Xu, K. Zhang, Y. Zhang, and J. Jiang, Packing fraction, tortuosity, and permeability of granular-porous media with densely packed spheroidal particles: Monodisperse and polydisperse systems, Water Resour. Res. **58**, e2021WR031433 (2022).

[62] T. Ahmed, *Reservoir Engineering Handbook* (Gulf Professional Publishing, Houston, TX, 2018).